

Object Re-identification via Spatial-temporal Fusion Networks and Causal Identity Matching

Hye-Geun Kim, *Student Member, IEEE*, Yong-Hyuk Moon, and Yeong-Jun Cho, *Member, IEEE*

Abstract—Object re-identification (ReID) in large camera networks has many challenges. First, the similar appearances of objects degrade ReID performances. This challenge cannot be addressed by existing appearance-based ReID methods. Second, most ReID studies are performed in laboratory settings and do not consider ReID problems in real-world scenarios. To overcome these challenges, we introduce a novel ReID framework that leverages a spatial-temporal fusion network and causal identity matching (CIM). The framework estimates camera network topology using the proposed adaptive Parzen window and combines appearance features with spatial-temporal cue within the Fusion Network. It achieved outstanding performance across several datasets, including VeRi776, Vehicle-3I, and Market-1501, achieving up to 99.70% rank-1 accuracy and 95.5% mAP. Furthermore, the proposed CIM approach, which dynamically assigns gallery sets based on the camera network topology, further improved ReID accuracy and robustness in real-world settings, evidenced by a 94.95% mAP and 95.19% F1 score on the Vehicle-3I dataset. The experimental results support the effectiveness of incorporating spatial-temporal information and CIM for real-world ReID scenarios regardless of the data domain (e.g., vehicle, person).

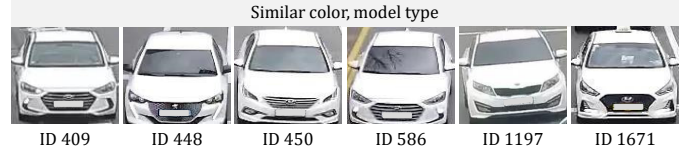
Index Terms—Re-identification, Real-world surveillance system, Spatial-temporal information, Adaptive Parzen window, Fusion network, Causal Identity Matching

I. INTRODUCTION

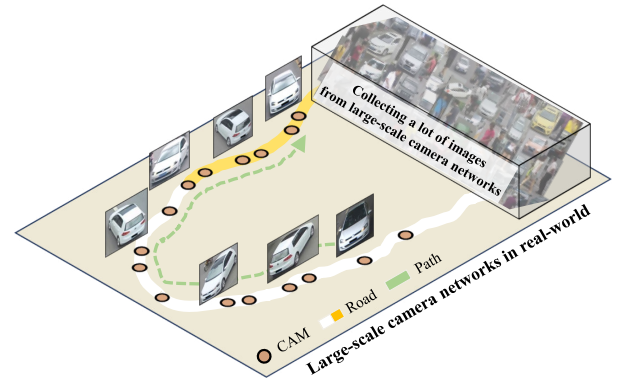
AN increasing number of surveillance cameras have been installed in public places for safety, traffic monitoring, and security. However, monitoring all cameras entails significant human effort and resources. Re-identification (ReID) can be applied to automatically track targets across multiple non-overlapping cameras to reduce human effort. In general, most studies have focused on the visual appearance of a target to perform ReID. For example, many studies [1], [2] have proposed feature learning methods to represent the appearance of a target. Similarly, to measure feature distance between queries and gallery images effectively, metric learning methods [3], [4] have also been proposed. Recently, the ReID performance has been improved by learning visual features and distance metrics with developments in deep learning [5], [6]. These appearance-based methods are robust to pose variations, viewpoint changes, and illumination changes.

Nevertheless, appearance ambiguity caused by objects with similar appearances is still not alleviated. As shown in Fig. 1a,

Hye-Geun Kim is with the Department of AI convergence, Chonnam National University, South Korea. Yong-Hyuk Moon is with Electronics and Telecommunications Research Institute, Daejeon, South Korea. Yeong-Jun Cho is with the Department of AI convergence, Chonnam National University, South Korea. (e-mail: yj.cho@chonnam.ac.kr).



(a) Appearance ambiguity in ReID



(b) High computational complexity

Fig. 1: Challenges in object re-identification

vehicles are difficult to match exactly because of their similar appearance due to the same model types. Compared to vehicles, people have relatively distinct features but have similar appearances due to the same clothes. In addition, the appearance of a large number of objects in multiple cameras causes higher computational complexity and lower identification performance because the number of objects with similar appearance to the target increases (Fig. 1b). Thus, relying only on the target appearance is ineffective for the object ReID problem.

Recently, ReID studies using additional spatial and temporal information to alleviate appearance ambiguity [7]–[10] have been proposed. Researchers have built a camera-network topology that explains the spatial and temporal relationships between cameras and used the topology to reduce redundant retrieval time ranges for queries. While the methods can potentially improve appearance-based ReID models [5], [6], they still have limitations. Their camera network topology modeling approaches are too simple, and integrating the appearance model with spatial-temporal information lacks optimization.

In addition, most ReID studies have not considered applying ReID in real-world scenarios. For example, videos continuously come in real-time from each camera. However, most

ReID studies [5], [11] have performed ReID on fixed and refined query-gallery sets, which are very clean and easy to handle. These laboratory settings are difficult to implement in real-world environments and require additional processes such as object appearance management and query-gallery sets management. In summary, previous studies did not fully consider spatial-temporal dependencies between cameras and real-world scenarios.

To consider the spatial and temporal dependencies between cameras, we proposed a spatial-temporal fusion network (FusionNet) in our previous study [12]. For training FusionNet, we proposed a novel adaptive Parzen window method robust to outliers and sparse responses between camera pairs (Section III-A). It can effectively manage different connection strengths of camera pairs for reliable camera network topology estimation. After estimating the topology, we trained a FusionNet to optimally combine appearance similarity and spatial-temporal probabilities (Section III-B). In this study, we extend our study [12] to explore ReID problems in real-world scenarios extensively. To this end, we first build a new large-scale vehicle ReID dataset called *Vehicle-3I*, including 2,038 identities captured by 11 synchronized cameras installed in three different intersections (Section V). Unlike many public datasets [13], [14] that provide only cropped image patches, it provides full-frame videos.

Furthermore, we focus on critical and practical issues for ReID in real-world scenarios. Issue 1) Each identity has a set of multiple appearances in the video. Therefore, an appearance management process and ID-to-ID re-identification should be addressed. Issue 2) The query and gallery cannot be predefined as in previous studies. Instead, the query and gallery are determined dynamically based on the target objects (query), and their ReID results within the camera network. In Section IV, we propose the appearance management and ID-to-ID ReID methods by considering multiple appearances of each identity in the video. Also, we perform Causal Identity Matching (CIM), which dynamically controls the query and gallery sets according to the camera connection causality.

To evaluate the proposed spatial-temporal fusion network, we tested the *VeRi776* [14], *Vehicle-3I* vehicle ReID datasets and *Market-1501* [13] person ReID dataset. We evaluated the effectiveness of the adaptive Parzen window and FusionNet, and the proposed spatial-temporal fusion network achieved the best performances in all datasets for the rank-1 accuracy (99.70%, 89.22%, 99.11%) and mean average precision (mAP) (91.71%, 83.62%, 93.80%). The results support that our methods can significantly improve the re-id performance regardless of the data domain (e.g., vehicle, person). We additionally perform CIM and evaluate the proposed methods for real-world scenarios; the proposed methods achieved the superior performances in *Vehicle-3I* dataset for the 94.95% mAP and 95.19% F_1 score.

The contributions of our study are as follows:

- Proposing FusionNet that combines two different similarities (appearance and spatial-temporal).
- Creating a new large-scale vehicle ReID dataset.
- Considering real-world ReID scenarios and performing extensive evaluations.

- Achieving superior performances on both vehicle and person ReID tasks.

II. RELATED WORKS

A. Appearance-based ReID

Most ReID studies have focused on developing visual representations of images to distinguish their appearance. There has been extensive research on metric learning and feature learning methods to achieve this objective. For metric learning, the widely studied approach has been learning the Mahalanobis distance [3], [4]. In particular, the optimization of triplet loss for deep metric learning [5], [15], [16] has shown outstanding performance in ReID tasks. Ghosh et al. [6] have introduced Relation Preserving Triplet Mining (RPTM), a scheme for feature matching-guided triplet mining that ensures triplets preserve natural subgroupings in object IDs.

Ahmed et al. [1] initially employed a deep convolutional neural network (CNN) architecture to capture local relationships between two input images based on mid-level features. Chen et al. [2] improved the CNN-based ReID by proposing a deep pyramid feature learning CNN, which is capable of learning scale-specific discriminative features. Similarly, efforts have been made by studies [15], [17] to extract robust local features. To capture more appearance details, Khamis et al. [18] utilized the attributes of targets for ReID. Recently, He et al. [11] proposed TransReID, which is the first attempt to use a transformer to learn robust features from the image patches and Chen et al. [19] utilized Swin Transformer [20] as a backbone for downstream ReID tasks.

CLIP-ReID, which fine-tunes the initialized visual model using the image encoder in CLIP, was proposed by Li et al. [21] for a better visual representation. Additionally, there have been studies [22], [23] focusing on pre-training methods that aim to overcome the domain gap in ReID tasks.

Furthermore, several approaches [24]–[27] have utilized extra cues, such as human pose and body parts, to address pose variations and occlusion issues. Similarly, studies [28], [29] have aimed to improve the quality of visual representation through additional identity-guided human semantic parsing and multi-head attention. Nevertheless, alleviating appearance ambiguity is still challenging when relying only on appearance for ReID.

B. Spatial-temporal ReID

Spatial-temporal information from cameras and target objects has been utilized in many studies to address the constraints of appearance-based ReID. Generally, these studies have taken an appearance-based ReID model as the baseline and leveraged spatial and temporal information. In spatial-temporal ReID, two main challenges occur: 1) estimating spatial-temporal information (the camera network topology) in given camera networks, and 2) utilizing the estimated camera network topology for ReID.

Many studies have attempted to estimate the camera network topology by designing accurate transition time distributions of targets, such as persons and vehicles. For instance, Huang et al. [9] utilized a spatial-temporal model leveraging

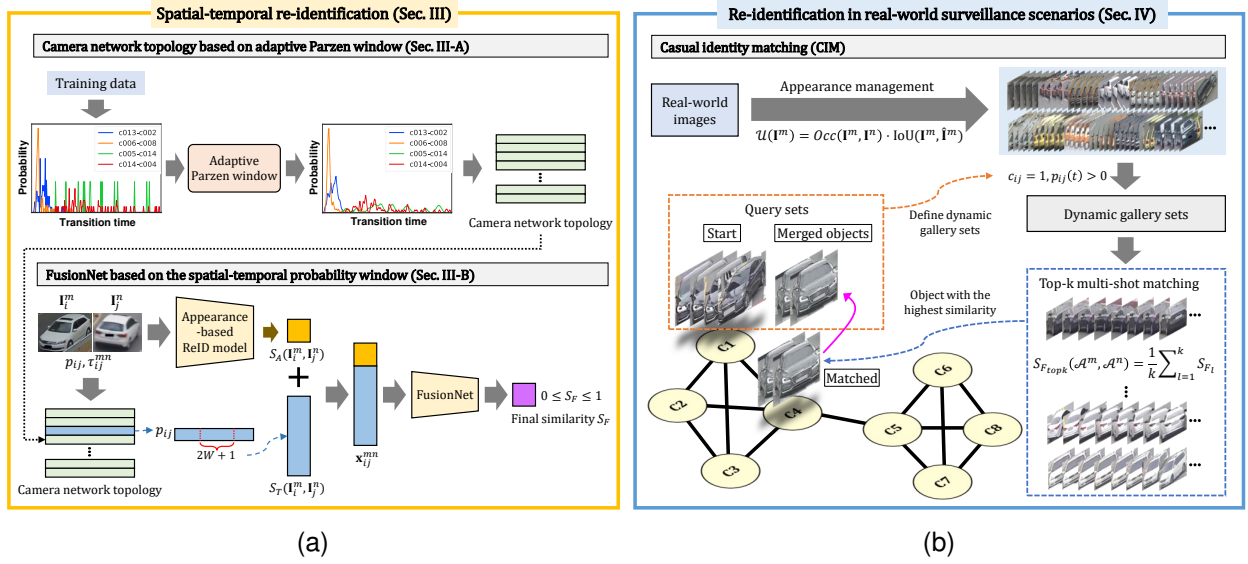


Fig. 2: The overall ReID methods for object re-identification with spatial-temporal information in real-world scenarios.

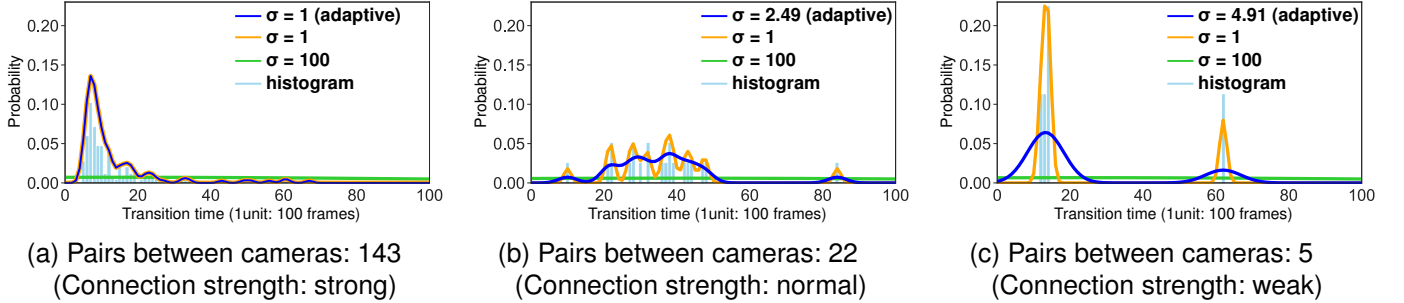


Fig. 3: Examples of estimated transition time distributions between camera pairs. Each bin covers 100 frame ranges. Solid blue lines (—) mark the estimated distribution (p_{ij}) from the histogram (h_{ij}) by the proposed adaptive Parzen window (best viewed in color).

vehicle pose view embedding and Wang et al. [10] proposed the Histogram-Parzen method to estimate spatial-temporal probability distributions. Additionally, Liu et al. [14], [30] proposed a progressive vehicle ReID that applying simple spatial-temporal information. Similarly, studies [7], [31]–[33] have utilized estimated spatial-temporal information to filter out irrelevant gallery images. Furthermore, Shen et al. [8] proposed a Siamese-CNN+Path-LSTM network that predicts the path through visual feature information and spatial-temporal information.

While numerous spatial-temporal ReID methods have been proposed, there are still some limitations. First, the methodologies for estimating spatial-temporal models are simplistic. For example, many methods [7], [14], [30], [31] have built object transition time distributions based on the positive responses between cameras, but noisy and sparse responses make the estimated distributions unreliable. Second, the utilization of spatial-temporal information is not optimized. Some studies [9], [10], [33] have merged both probabilities (i.e., appearance and spatial-temporal) with same importance to obtain the joint probability. Similarly, many methods [7], [31]–[33] have applied spatial-temporal information to reduce the

search range or perform re-ranking of the initial ReID results.

III. SPATIAL-TEMPORAL RE-IDENTIFICATION BASED ON FUSIONNET

To address the challenges in ReID, we analyzed the characteristics of objects in camera networks. First, many objects show similar or the same appearances in large-scale camera networks. For example, people can appear similar due to wearing the same clothes (e.g., uniforms and belongings). Especially in the vehicle ReID task, vehicles can look the same according to their model types. Second, the movements of objects between non-overlapping cameras are predictable. E.g., vehicles can only move along roads and highways, rarely deviating from existing roads. Compared to vehicles, people show more complex transition patterns across cameras, but people's paths are also generally established along the side-walks and aisles. To summarize, objects show high appearance ambiguities but predictable movements. Therefore, relying only on appearance differences between objects is not effective for the ReID tasks.

Based on these observations, we additionally exploited spatial and temporal relationships between cameras, called a

camera network topology. As shown in Fig. 2a, the proposed spatial-temporal ReID framework consists of two parts: 1) camera network topology estimation based on the adaptive Parzen window, 2) the fusion network on the spatial-temporal probability window. We first built the topology based on the proposed adaptive Parzen window (Section III-A). Then, we trained a FusionNet that optimally combines visual similarity and the camera network topology information for the final ReID prediction (Section III-B).

A. Adaptive Parzen window

The camera network topology represents the spatial-temporal relationships and connections between cameras, which can be represented by a graph $\mathbf{G} = (\mathbf{V}, \mathbf{E})$. The vertices \mathbf{V} represent the cameras, and the edges \mathbf{E} represent the distribution of object transition time. If there are N_{cam} cameras in the network, the topology is represented as follows:

$$\begin{aligned} \mathbf{V} &\in \{c_i | 1 \leq i \leq N_{\text{cam}}\}, \\ \mathbf{E} &\in \{p_{ij} | 1 \leq i \leq N_{\text{cam}}, 1 \leq j \leq N_{\text{cam}}, i \neq j\}, \end{aligned} \quad (1)$$

where c denotes a camera, and p_{ij} denotes the object transition time distribution between camera pairs c_i and c_j .

We build the transition time distribution p_{ij} by leveraging positive pairs from all camera pairs in the training dataset. Using the multiple time differences (Δt) of positive pairs, we initially generated a histogram of the transition time h_{ij} , which is illustrated by the cyan vertical lines (—) in Fig. 3. Cho et al. [7] proposed connectivity checking criteria for determining if a pair of cameras are connected by fitting a Gaussian model to the histogram h_{ij} . However, this parametric method followed strong assumptions and had difficulty handling outliers and the sparsity of the histogram. Inspired by [10], a Parzen window method can be applied to the initial histograms, and we estimated the probability density function (PDF) of the transition time in a non-parametric manner as follows:

$$p_{ij}(\tau) = \frac{1}{Z} \sum_l h_{ij}(\tau) K(l - \tau), \quad (2)$$

where τ is an index of the distribution, $Z = \sum_l p_{ij}(\tau)$ represents a normalized factor, and $K(\cdot)$ is a kernel function. For the kernel K , we used the Gaussian function, as follows:

$$K(x) = \frac{1}{\sqrt{2\pi}\sigma} \exp\left(-\frac{x^2}{2\sigma^2}\right), \quad (3)$$

where σ is a standard deviation.

Estimating continuous PDFs from discrete histograms efficiently using the Parzen window method is unreasonable when employing a single kernel across diverse histograms from various camera pairs. The strength of the spatial-temporal connection between cameras can be determined by the number of objects passing through those cameras during a certain period [7]. For example, weak connectivity is indicated by few positive pairs between two cameras. However, the Parzen window method extremely enlarges those small responses with a small σ value, as depicted in the orange line (—) in Fig. 3c. In that case, it is better to use a large σ value to avoid overfitting the distribution for noise and outliers.

In contrast, if there are many positive pairs between the cameras, the connectivity should be strong. On the other hand, when using a large σ value, the resulting distribution becomes uniform, failing to capture any meaningful spatial and temporal relationships between the cameras, as displayed by the green line (—) in Fig. 3a. In that case, it is better to use a relatively small σ value to reflect temporal information between cameras. Therefore, selecting the appropriate σ value is important for the quality of the estimated distribution (p_{ij}).

To overcome the limitation of the original Parzen window method [10], we newly propose an adaptive Parzen window by setting various σ_{ij} values for the camera pairs (c_i, c_j) . To this end, we designed an adaptive standard deviation according to the different strengths of the camera connectivity as follows:

$$\sigma_{ij} = \max\left(\alpha \exp\left(\frac{-N_{ij}}{\beta}\right), 1\right), \quad (4)$$

where N_{ij} denotes the number of positive object pairs between camera c_i and c_j . In addition, α is a scale factor determining the maximum range of σ_{ij} , and β is a smoothness factor that adjusts the sensitivity of σ_{ij} . The minimum value of σ_{ij} cannot be less than 1 unit of the histogram. Then, the values of σ_{ij} lie on $[1, \alpha]$.

By considering the camera indexes, Eq. 2 and Eq. 3 are reformulated as follows:

$$p_{ij}(\tau) = \frac{1}{Z} \sum_l h_{ij}(\tau) K_{ij}(l - \tau), \quad (5)$$

$$K_{ij}(x) = \frac{1}{\sqrt{2\pi}\sigma_{ij}} \exp\left(\frac{-x^2}{2\sigma_{ij}^2}\right). \quad (6)$$

Therefore, we can estimate reliable distributions (p_{ij}) from the initial discrete histograms (h_{ij}) by considering the connectivity between cameras. The blue lines (—) in Fig. 3 are our results based on the adaptive Parzen window.

B. Fusion Network

The baseline for the proposed ReID framework can be any appearance-based ReID method, which estimates appearance similarities between images. Object images from each camera pair (c_i, c_j) are represented as $\mathbf{I}_i^m, \mathbf{I}_j^n$, where m and n are the image indexes. Then, the appearance-based ReID methods estimate the visual similarity between two images as $S_A(\mathbf{I}_i^m, \mathbf{I}_j^n)$ that lies on $[0, 1]$. The proposed framework is not reliant on typical appearance-based models.

To perform spatial-temporal ReID, Cho et al. [7] used only camera network topology to limit the gallery search range, effectively reducing the complexity of ReID. However, the spatial-temporal probability does not affect the final similarity. In contrast, previous studies [9], [10], [33] have merged both probabilities (i.e., appearance and spatial-temporal) with the same importance to obtain the joint probability. However, they neglected two key points. First, the domains of each probability are not the same. Second, both appearance and spatial-temporal probabilities can be imperfect. Hence, simply merging these probabilities is unreasonable.

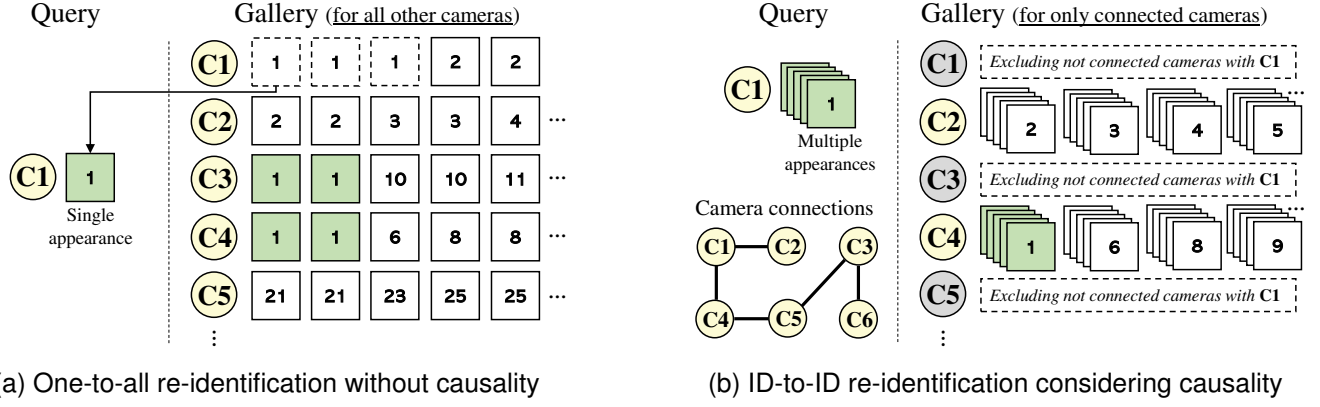


Fig. 4: Comparisons of re-identification methodologies. Circles and boxes denote cameras and appearances, respectively. The number in the box denotes the ID of the appearance. Boxes filled with olive color are true positives with the query. Boxes with a dotted line indicate excluded appearances from the gallery. (a) One-to-all ReID using only a single appearance for the query performs many redundant and duplicated comparisons. It even compares different objects within the same camera. (b) ID-to-ID ReID uses multiple appearances and considers causality to determine the gallery.

In this study, we optimally combined visual similarities $S_A(\mathbf{I}_i^m, \mathbf{I}_j^n)$ and estimated spatial-temporal probability distributions $p_{ij}(\tau)$ through the fusion network named FusionNet. An input vector of the network for two images $(\mathbf{I}_i^m, \mathbf{I}_j^n)$ in the camera pair (i, j) can be represented by

$$\mathbf{x}_{ij}^{mn} = [S_A(\mathbf{I}_i^m, \mathbf{I}_j^n), S_T(\mathbf{I}_i^m, \mathbf{I}_j^n)], \quad (7)$$

where S_A is an appearance similarity, and S_T is a spatial-temporal vector. The S_T vector between the images is defined by

$$S_T(\mathbf{I}_i^m, \mathbf{I}_j^n) = \left[p_{ij}(\tau_{ij}^{mn} - W), \dots, p_{ij}(\tau_{ij}^{mn} - 1), p_{ij}(\tau_{ij}^{mn}), p_{ij}(\tau_{ij}^{mn} + 1), \dots, p_{ij}(\tau_{ij}^{mn} + W) \right], \quad (8)$$

the notation τ_{ij}^{mn} represents the time difference between two images \mathbf{I}_i^m and \mathbf{I}_j^n . The parameter W denotes the size of a time window. The range of the S_T vector depends on the value of W and is determined around distributions of $p_{ij}(\tau_{ij}^{mn})$. For example, when $W = 0$, S_T becomes a scalar value given by $S_T(\mathbf{I}_i^m, \mathbf{I}_j^n) = p_{ij}(\tau_{ij}^{mn})$. If $W > 0$, the S_T vector has a dimension of $2W + 1$. The value of W can be adjusted to determine the amount of spatial-temporal information to be provided to the FusionNet. Then, the dimension of the input vector \mathbf{x}_{ij}^{mn} for the FusionNet is $2W + 2$.

The FusionNet was designed based on a simple multi-layer perception. We found empirically that the FusionNet does not require a sophisticated deep neural network structure to estimate the final similarity. The network has one hidden layer with several nodes and a one-dimensional output layer, as illustrated in Fig. 2a. For the activation function, we used the Rectified Linear Unit (ReLU) for nodes in the hidden layer and the sigmoid function for the output node. Then, the final output of the FusionNet, $S_F(\mathbf{I}_i^m, \mathbf{I}_j^n)$, is within the range $[0, 1]$. To train the network, we optimized the binary cross-entropy loss as defined by

$$\mathcal{L} = \sum_k y_k \log S_F(k) + (1 - y_k) \log(1 - S_F(k)), \quad (9)$$

where k represents the index of the training image pair, and $y_k \in [0, 1]$ denotes the ground truth of the k -th image pair.

IV. RE-IDENTIFICATION IN REAL-WORLD SURVEILLANCE SCENARIOS

Previous studies have evaluated their methods using a fixed and refined gallery set. They selected a query image from the gallery and compared it with all other images in the gallery, which is a one-to-all single-shot comparison. This evaluation process is repeated until all queries are compared, and then all the results are averaged to compute the final ReID performance. Note that the gallery set contains multiple appearances for a single identity, leading to many duplicated comparisons as shown in Fig. 4a. These laboratory evaluation settings are not suitable for real-world scenarios at all, since multiple appearances of the object do not need to be evaluated individually.

In real-world surveillance scenarios, we have to consider additional issues beyond the laboratory settings. First, each identity can have multiple appearances in the video, and their appearances should be evaluated in ID-to-ID manner as explained in Fig. 4b. Second, the query and gallery sets are not fixed throughout all the test processes; instead, they can change according to the target objects and matching causality. Considering the issues in real-world scenarios, we additionally propose causal identity matching (CIM) from our previous work [12]. CIM includes three different methods (Section. IV-A– IV-C) for effective ReID in real-world scenarios. The overall framework of CIM is illustrated in Fig. 2b.

A. Appearance management for each object

As mentioned above, each object has multiple appearances along with its trajectory in the sequence. Assuming that a camera captures multiple frames per second, we can collect various

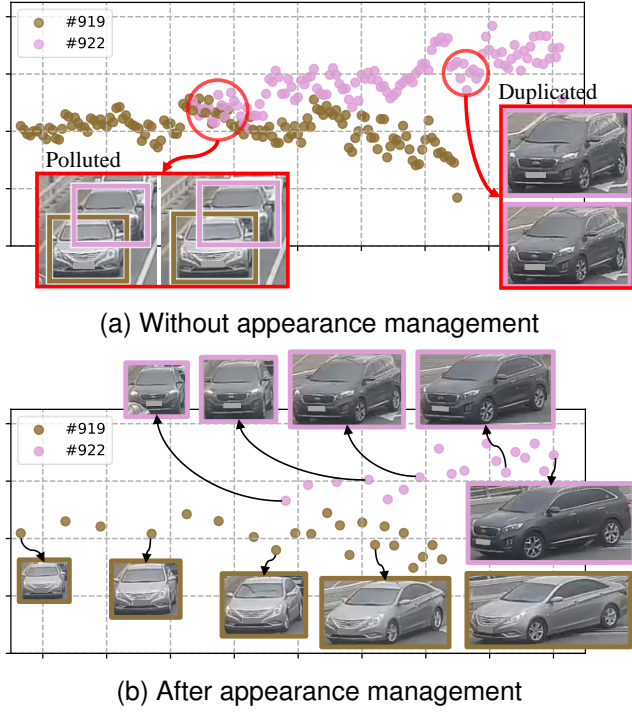


Fig. 5: Features distributions of objects. Example image patches reflect actual sizes of them.

images, which is advantageous for ReID. However, this also requires a significant amount of computation. We observed that many of the appearances are unreliable and redundant in many cases. For example, when another object occludes an object, the appearances of different objects can become very similar, resulting in unreliable appearances. Additionally, when an object remains in the same location and pose for a long period, multiple appearances of the object are identical, leading to redundant appearances. We here define the bounding box of the m -th object image \mathbf{I}^m as $\text{bbox}(\mathbf{I}^m) = [x^m, y^m, w^m, h^m]$. We omit camera indexes i, j for convenience at this step. In the video, the m -th object contains a set of appearances as

$$\mathcal{A}^m = \{\mathbf{I}^{m,1}, \mathbf{I}^{m,2}, \dots, \mathbf{I}^{m,N_m}\}, \quad (10)$$

where N_m is the total number of the appearances in m -th object.

Inspired by [34], we perform appearance management for each object. To detect occluded unreliable objects, the occlusion ratio between two different objects is calculated based on Intersection over Union (IoU) by $\text{IoU}(\mathbf{I}^m, \mathbf{I}^n) = \frac{\text{bbox}(\mathbf{I}^m) \cap \text{bbox}(\mathbf{I}^n)}{\text{bbox}(\mathbf{I}^m) \cup \text{bbox}(\mathbf{I}^n)}$. In general, surveillance cameras are installed at a high position from the ground, looking down at an angle. This means that an overlapping object with a larger y -value is occluding another object. Therefore, we designed the occlusion ratio of m -th object by

$$\text{Occ}(\mathbf{I}^m, \mathbf{I}^n) = \begin{cases} \text{IoU}(\mathbf{I}^m, \mathbf{I}^n), & \text{if } y^m < y^n \\ 0, & \text{otherwise} \end{cases} \quad (11)$$

where $m \neq n$. When there are multiple bounding boxes occluding \mathbf{I}^m , the largest value among them will be used as the final occlusion ratio.

Next, we measure a self-overlapping ratio to prevent duplicate appearances from being included in the set \mathcal{A}^m . For simplicity, let $\hat{\mathbf{I}}^m \in \mathcal{A}^m$ is the last appearance in the set \mathcal{A}^m . Then, the self-overlapping ratio calculated by $\text{IoU}(\mathbf{I}^m, \hat{\mathbf{I}}^m)$. Finally, we merge two ratios to define the appearance unreliability score of \mathbf{I}^m by

$$\mathcal{U}(\mathbf{I}^m) = \text{Occ}(\mathbf{I}^m, \mathbf{I}^n) \cdot \text{IoU}(\mathbf{I}^m, \hat{\mathbf{I}}^m). \quad (12)$$

It reflects both appearance occlusion and duplication. Based on this, we can easily reject unreliable appearances by selecting only those with the lowest scores.

Figure 5 illustrates the feature distributions of four different objects. Without the proposed appearance management, they are not clearly separated in the feature space due to occlusions. Furthermore, each object has similar and redundant appearances when standing at the traffic signal. After performing appearance management, the unreliable appearances were appropriately removed, preserving the original distributions with a much smaller number of appearances.

B. Top- k Multi-shot Matching

After appearance management, objects contain more reliable appearances in their appearance sets. In order to compare two different appearance sets, many traditional multi-shot matching ReID methods have tried minimum (max) and average (avg.) aggregation approaches in general. However, the ‘max’ approach, which selects only the maximum similarity value among multiple appearance comparison results, can result in highly biased final outcomes. On the other hand, the ‘avg.’ approach, which averages all the comparison results, can result in overly smoothed final outcomes.

To mitigate these risks, we perform Top- k multi-shot matching to compare two different appearance sets. Given two different appearance sets $\mathcal{A}^m, \mathcal{A}^n$ with their cardinalities $|\mathcal{A}^m| = N_m, |\mathcal{A}^n| = N_n$, there are $N_m \times N_n$ appearance comparisons. Based on the FusionNet in Section III-B, the appearance similarities between the two sets are represented by

$$S_F(\mathcal{A}^m, \mathcal{A}^n) = \{S_F(\mathbf{I}^{m,1}, \mathbf{I}^{n,1}), \dots, S_F(\mathbf{I}^{m,N_m}, \mathbf{I}^{n,N_n})\}, \quad (13)$$

Sort $S_F(\mathcal{A}^m, \mathcal{A}^n)$ in descending order and then we get

$$S_{F_{\text{sorted}}}(\mathcal{A}^m, \mathcal{A}^n) = \{S_{F_1}, S_{F_2}, \dots, S_{F_{N_m \times N_n}}\}, \quad (14)$$

Finally, top- k multi-shot matching is calculated by

$$S_{F_{\text{top}k}}(\mathcal{A}^m, \mathcal{A}^n) = \frac{1}{k} \sum_{l=1}^k S_{F_l}. \quad (15)$$

By adjusting k , we can determine how many results to utilize in the multi-shot appearance comparison. We empirically set the value of k around 5, which improved ReID performances as in Table. VII. The proposed top- k approach is quite simple but effective. It does not require complex structures for handling multi-shot comparisons like video-based ReID methods [35], [36] but can utilize single-shot baselines. In addition, it implements other approaches by setting $k = 1$ for the ‘max’ approach and $k = N_m \times N_n$ for the ‘avg.’ approach.

C. Causal Identity Matching (CIM)

In Section III-A, camera network topology was built as $\mathbf{G} = (\mathbf{V}, \mathbf{E})$, and FusionNet was trained based on this topology. The topology includes transition time distributions p_{ij} between all possible camera pairs, regardless of their connection strengths, enabling FusionNet to learn these strengths for determining the similarity S_F . In real-world scenarios, we focus more on the target object (i.e., query) and its causality in the camera networks \mathbf{G} . The causality indicates where the target object is currently and where it is likely to move next based on the topology. In this setting, the query and gallery sets should not be fixed or pre-defined but should dynamically change according to the ReID results at each step.

To consider aforementioned conditions and perform the causal identity matching (CIM), we first define camera adjacent matrix by $\mathbf{C} \in \{c_{ij} | 1 \leq i \leq N_{cam}, 1 \leq j \leq N_{cam}\}$, where i, j are camera indexes, and c_{ij} denotes a binary adjacent flag between cameras. When cameras c_i and c_j are adjacent, the flag is set to $c_{ij} = 1$; otherwise, it is set to $c_{ij} = 0$. We set all the diagonal terms in \mathbf{C} to $c_{ii} = 0$. Given multiple object paths, we can simply find adjacent cameras and overall connections between them. For example, assuming that there are multiple object paths such as $(c_1 \rightarrow c_2 \rightarrow c_3)$, $(c_2 \rightarrow c_3)$, $(c_2 \rightarrow c_4)$, and $(c_4 \rightarrow c_2)$; then the camera adjacent matrix is defined by

$$\mathbf{C} = \begin{bmatrix} 0 & 1 & 0 & 0 \\ 0 & 0 & 1 & 0 \\ 0 & 0 & 0 & 1 \\ 0 & 1 & 0 & 0 \end{bmatrix}. \quad (16)$$

Note that the matrix can be asymmetric when considering a bidirectional camera network topology. More reliable adjacent connections can be estimated by voting on sufficient numbers of paths. In addition, unnecessary paths can be further removed through post-processing algorithms like transitive reduction [37]¹. Excluding redundant paths helps to improve the overall efficiency of ReID.

Next, we assign dynamic gallery sets for the target object. Imagine that there is a target object (query) in the camera c_1 . Then, the gallery set of the query comes from the cameras adjacent to c_1 by finding $(c_{1j} = 1)$ in \mathbf{C} . Furthermore, the objects in the gallery are confirmed by referring to the corresponding transition time distributions $p_{1j}(t)$. Only the objects in the camera j within the appearing time t that satisfy $p_{1j}(t) > 0$ are included in the gallery. Through this process, we can causally assign the gallery set using \mathbf{C} and reduce many unnecessary matching candidates based on $p_{ij}(t)$.

An object in the gallery with the highest similarity to the query is considered a successful match, and the query is merged with the re-identified object. This increases the diversity of the query's appearance, making the next step of ReID much more advantageous. In other words, although a single camera can only capture fixed poses of the object, progressive query merging easily overcomes this limitation. In this way, the updated query is used to progressively perform ReID on the

next adjacent cameras, and the gallery is adaptively determined by \mathbf{C} and p_{ij} as well.

V. DATASETS

For various experiments, we used VeRi776 [14] vehicle re-identification (ReID) datasets, and Market-1501 [13] person ReID dataset. In addition, to validate the proposed methods in a real-world scenario, we newly constructed a Vehicle-3I vehicle ReID dataset.

- VeRi776 [14] dataset contains over 49,000 images of 776 different vehicle identities (IDs) captured by 20 non-overlapping synchronized cameras. Each vehicle passes through 2 to 18 cameras with various viewpoints, illuminations, resolutions, and occlusions.
- Vehicle-3I is our new dataset for vehicle ReID, as summarized in Table I and Fig. 6. 11 synchronized cameras captured vehicles at three different intersections. The dataset contains over 40,000 images with 2,038 IDs. The three intersection scenarios reflect the complexity and challenges of real-world traffic environments. Unlike public datasets [13], [14] providing only cropped image patches, it provides full-frame videos. Furthermore, compared to VeRi776 [14], most vehicles in Vehicle-3I are achromatic (94.21%), which poses a significant challenge for ReID (Fig. 7). Achromatic colors without hue, such as white, gray, and black, are difficult to discriminate under varying illumination conditions.
- Market-1501 [13] contains over 32,000 images of 1,501 different people IDs captured by six non-overlapping synchronized cameras. Each image contains object IDs, timestamps (frame No.), and camera IDs. On average, each person is represented by 3.6 images per viewpoint.

VI. EXPERIMENTAL RESULTS

A. Settings

To estimate the camera network topology $\mathbf{G} = (\mathbf{V}, \mathbf{E})$, we used training datasets (576 IDs in VeRi776, 1,630 IDs in Vehicle-3I and 751 IDs in Market-1501). Among them, 90% of the training data were used for appearance-based ReID model training and the remaining 10% were used for FusionNet training. Note that the object identities (IDs) were completely separated for each training task.

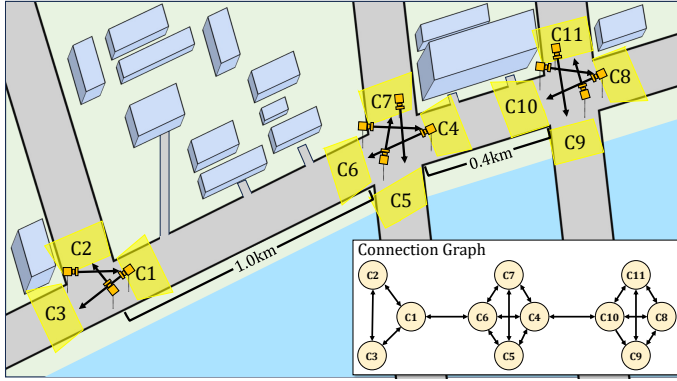
In VeRi776 with 20 cameras ($N_{cam} = 20$), the estimated camera network topology contains 400 object transition time distributions (p_{ij}). Among them, 380 distributions are between different camera pairs (i.e., p_{ij} , where $c_i \neq c_j$), and each distribution has 300 bins, each covering 100 frame ranges. All distributions were estimated based on the proposed adaptive Parzen window. By performing the same processes, we also estimated the camera network topology of Vehicle-3I and Market-1501.

For the appearance-based ReID model in our framework, we trained FastReID [5] and SOLIDER [19] to extract the appearance similarity. The hyper parameters of FastReID in both datasets are as follows: epoch – 60, batch size – 64. For the vehicle ReID task, a simple ResNet-50 [38] was utilized

¹When there is a new path $(c_1 \rightarrow c_3)$, it does not assign $c_{13} = 1$, immediately. Instead, the algorithm tries to infer if there is an intermediate vertex c_2 between c_1 and c_3 from numerous training paths.

Index	Cam 1	Cam 2	Cam 3	Cam 4	Cam 5	Cam 6	Cam 7	Cam 8	Cam 9	Cam 10	Cam 11	Total
# ID	456	240	494	570	696	430	667	788	159	843	408	2,038
# Annotated box	4,905	2,667	5,200	3,524	3,603	2,466	3,510	3,975	1,077	6,509	2,905	40,341
# Frames	17,979	17,973	17,986	14,300	17,997	17,958	17,991	17,961	17,987	17,963	17,883	-
Duration	19m 58s	19m 58s	19m 59s	15m 53s	19m 59s	19m 57s	19m 59s	19m 57s	19m 59s	19m 57s	19m 52s	-
Color (%)	□ 40.13	□ 38.75	□ 39.27	□ 39.47	□ 38.22	□ 41.16	□ 41.53	□ 37.69	□ 39.62	□ 37.01	□ 41.67	□ 38.96
	■ 30.92	■ 30.42	■ 30.77	■ 35.79	■ 34.63	■ 30.23	■ 31.18	■ 36.42	■ 39.62	■ 36.18	■ 38.73	■ 34.40
	■ 22.81	■ 24.58	■ 24.09	■ 20.70	■ 21.70	■ 21.86	■ 21.14	■ 20.30	■ 15.09	■ 21.59	■ 15.93	■ 20.85
	■ 6.14	■ 6.25	■ 5.87	■ 4.04	■ 5.45	■ 6.75	■ 6.15	■ 5.59	■ 5.67	■ 5.22	■ 3.67	■ 5.79
Vehicle color statistics: □ White colors ■ Gray colors ■ Black colors ■ Other chromatic colors												

TABLE I: Details of our new vehicle ReID dataset (Vehicle-3I). Color (%) summarizes the statistics of vehicle colors of each camera. The proportion of achromatic vehicles such as white, gray, and black is much higher than that of chromatic colored vehicles.



(a) Layout and connection graph

CAM	1	2	3	4	5	6	7	8	9	10	11
1		54	130	21	13	137	37	10	0	14	1
2	32		42	3	9	27	11	0	0	0	0
3	157	63		16	4	91	24	10	0	10	1
4	80	25	55		120	82	67	130	1	202	27
5	25	15	7	113		25	313	79	0	113	14
6	164	53	107	54	19		103	33	1	52	3
7	34	7	25	32	1	33		18	0	35	9
8	41	14	27	148	63	46	34		19	233	42
9	0	0	0	0	0	0	0	27		0	39
10	60	20	37	253	108	67	61	232	4		35
11	13	4	8	91	40	18	21	68	36	114	

(b) Number of vehicle pairs between cameras

Fig. 6: Overall connections and vehicle flows in Vehicle-3I

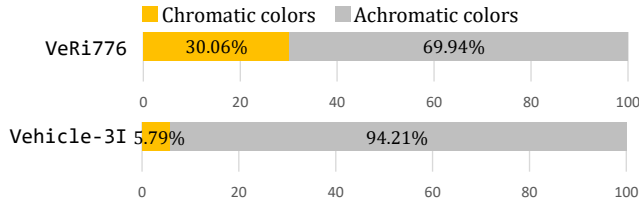


Fig. 7: Ratio of achromatic colors and chromatic colors in VeRi776 [14] and Vehicle-3I. White, gray and black colors are achromatic colors and the other colors are chromatic.

as the backbone network structure of FastReID. Meanwhile, for the Person ReID task, ResNet-101 with MGN [39] was utilized as the backbone network structure of FastReID.

The proposed FusionNet has a single hidden layer, and we designed the number of nodes in the hidden layer to be around 65% of the size of the input vector by rounding $(2(2W + 2)/3 + 1)$. Training parameters of FusionNet are as follows: epoch – 40, batch size – 128, learning rate – 0.001, optimizer – Adam. VeRi776 [14], Vehicle-3I and Market-1501 [13] have 200, 408, and 750 different IDs for the performance validation of methods and evaluation. We evaluated the rank-1 and rank-5 accuracy and mean average precision (mAP) based on the traditional 1-to-all single-shot comparison as described in Fig. 4.

B. Effects of FusionNet

In this experiment, we tested on VeRi776 [14], Market-1501 [13], and Vehicle-3I datasets to verify the effect of W value on FusionNet, and the results are shown in Table II. Additionally, we compared other methods such as *FastReID* [5] using only appearance similarities (S_A) between images. *FastReID* + Wang’s estimated the appearance similarity (S_A) based on FastReID [5] and simply combined the spatial-temporal similarity by $S_F = S_A(\mathbf{I}_i^m, \mathbf{I}_j^n) \cdot p_{ij}(\tau_{ij}^{mn})$, as in [10].

In VeRi776 [14], the *FastReID* [5] model, which uses only appearance information, achieved a rank-1 accuracy of 96.96% and an mAP of 81.91%. On the other hand, combining *FastReID* with Wang’s approach, which merges additional spatial-temporal similarity, improved the mAP of the appearance-based ReID [5] by 3.56%. However, the simple combination of these two different similarities using $S_A(\mathbf{I}_i^m, \mathbf{I}_j^n) \cdot p_{ij}(\tau_{ij}^{mn})$ is not yet optimized. The rank-1 and rank-5 performances decreased after implementing Wang’s approach in *FastReID* [5]. Using the proposed FusionNet, we achieved a significant improvement in ReID performance. For fair comparisons, we used *FastReID* [5] as the appearance model for our framework and trained FusionNet with 526 IDs for the appearance model and 50 IDs for FusionNet training. With W set to 10, FusionNet achieved the best performance in rank-1 accuracy at 99.70%, rank-5 accuracy at 99.82%, and mAP at 91.71%.

Methods	VeRi776 [14]				Vehicle-3I				Market-1501 [13]			
	No. of IDs	Rank-1	Rank-5	mAP	No. of IDs	Rank-1	Rank-5	mAP	No. of IDs	Rank-1	Rank-5	mAP
<i>FastReID</i> [5]	576 for	96.96	98.45	81.91	1,630 for	63.73	77.70	64.24	751 for	96.35	-	90.77
<i>FastReID</i> [5]+ <i>Wang's</i> [10]	Appearance	95.77	97.74	85.47	Appearance	81.37	88.60	66.34	Appearance	95.52	99.26	89.06
FusionNet ($W = 0$)	526 for Appearance	97.08	98.57	80.58	1,430 for Appearance	54.41	77.08	55.13	701 for Appearance	95.52	98.22	90.08
FusionNet ($W = 2$)		98.09	98.87	84.68		86.40	92.52	80.37		95.84	99.29	92.09
FusionNet ($W = 4$)		99.52	99.70	90.77		87.87	93.38	82.40		98.52	99.44	92.32
FusionNet ($W = 6$)		99.64	99.82	91.45		89.22	93.50	83.62		98.60	99.38	92.47
FusionNet ($W = 8$)	50 for FusionNet	99.64	99.82	91.55	200 for FusionNet	87.75	92.52	82.66	50 for FusionNet	97.27	99.52	92.83
FusionNet ($W = 10$)		99.70	99.82	91.71		88.85	92.65	83.36		99.11	99.58	93.80
FusionNet ($W = 12$)		99.64	99.82	91.57		88.48	93.01	82.91		98.84	99.52	93.52

TABLE II: ReID performances according to W values in FusionNet. The method *FastReID* [5] does not exploit spatial-temporal information S_T . *FastReID*+*Wang's* estimates the final similarity by $S_F = S_A(\mathbf{I}_i^m, \mathbf{I}_j^n) \cdot p_{ij}(\tau_{ij}^{mn})$, as in [10] and employed *FastReID* [5] for its appearance model. The best performances are marked in **bold**.

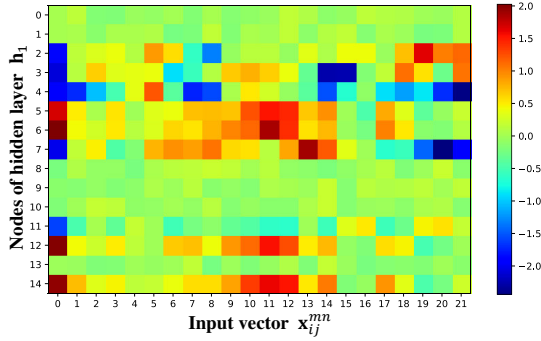


Fig. 8: A visualization of the trained weight vector (\mathbf{w}_1) between input and hidden layer (\mathbf{h}_1)

Except at $W = 0$, FusionNet outperformed other methods in all evaluation metrics (rank-1, -5, and mAP).

In Vehicle-3I, *FastReID* [5] using only appearance information achieved a rank-1 accuracy of 63.73% and mAP of 64.24%. The rank-1, rank-5, and mAP performances were increased after adopting *wang's* approach in *FastReID* [5]. This means that using spatial-temporal information in Vehicle-3I is also effective. Except $W = 0$, our proposed method significantly outperformed *FastReID* [5] and *FastReID* [5]+*Wang's* [10]. In $W = 6$, we achieved the best performance with 89.22% rank-1 accuracy, 93.50% rank-5 accuracy, and 83.62% mAP.

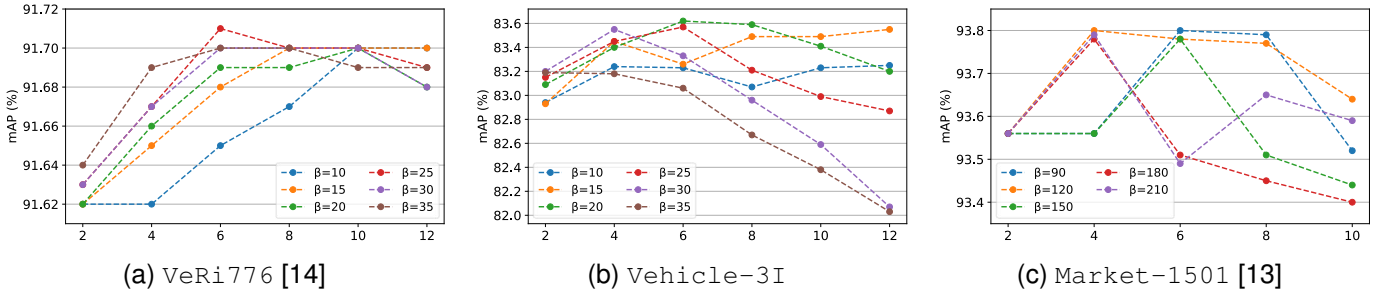
In Market-1501 [13], which is a person ReID dataset, *FastReID* [5] achieved a rank-1 accuracy of 96.35% and mAP of 90.77% using only appearance information. However, the rank-1 and mAP performances decreased after adopting *Wang's* approach into *FastReID* [5]. Nevertheless, the proposed framework significantly enhanced the ReID performance. FusionNet achieved the best performance with a rank-1 accuracy of 99.11%, rank-5 accuracy of 99.58%, and mAP of 93.8% when W was set to 10. This result supports that the proposed FusionNet can optimally combine different types of information, such as appearance similarity and spatial-temporal information. In addition, even if the training image for the appearance model was less utilized, it achieved superior performance compared to other methods.

Fig. 8 illustrates the trained weight vector (\mathbf{w}_1) between input and hidden layer (\mathbf{h}_1). The index of the nodes in \mathbf{h}_1 is denoted by the row numbers (0–14), and the index of the input vector \mathbf{x}_{ij}^{mn} is denoted by the column numbers (0–21). The first column (0 index) shows the weights for appearance similarity (S_A), which are notably more significant than other weights, indicating that the FusionNet has been effective in training the importance of appearance similarity (S_A). The weights in columns 1 to 21 are for spatial-temporal distribution (S_T). Interestingly, the weights from the 10th to 12th columns showed large magnitudes. This result suggests spatial-temporal information around the time difference (τ_{ij}^{mn}) between two images plays a key role in ReID. Additionally, FusionNet has a lightweight structure but effective.

We also tested the effect of hidden layer depth in FusionNet. We observed that the one hidden layer achieved the best mAP performance (91.71%). The performance decreased significantly to a 59.47% mAP score with a simple perceptron without a hidden layer. This means that a simple perceptron structure is not sufficient for combining appearance similarity and spatial-temporal information. Interestingly, increasing the depth of hidden layers did not lead to an improvement in mAP score; relatively, the mAP scores tended to decrease, E.g., 2-layer: 91.22%, 3-layer: 91.28%, 4-layer: 91.22%. It suggests that a large depth of hidden layers is not necessary, and one hidden layer is sufficient for learning the relationships between appearance similarity and spatial-temporal similarity.

C. Effects of adaptive Parzen window

We evaluated various factors for the proposed adaptive Parzen window method, such as the scale factor α and smoothness factor β in Eq. 4. We set $W = 10$ for FusionNet on VeRi776 [14] and Market-1501 [13] and set $W = 6$ on Vehicle-3I for FusionNet. Fig. 9 illustrates the mAP according to the α and β factors. When the scale factor $\alpha = 6$, and the smoothness factor $\beta = 25$, the proposed framework achieved the best mAP performance on VeRi776 [14]. In the same way, the proposed framework achieved the best mAP performance on all datasets with $\alpha = 6, \beta = 20$ on Vehicle-3I and $\alpha = 4, \beta = 120$ on Market-1501 [13]. Note that ReID performances do not significantly change with

Fig. 9: Performance according to α and β factors of the adaptive Parzen window.

Dataset	VeRi776 [14]		
Methods	Rank-1	Rank-5	mAP
Fixed $\sigma = 1$	99.70	99.82	91.57
Fixed $\sigma = 5$	99.52	99.70	91.43
Fixed $\sigma = 10$	99.28	99.76	91.28
Fixed $\sigma = 100$	98.81	99.46	86.62
Adaptive σ (ours)	99.70	99.82	91.71

Dataset	Vehicle-3I		
Methods	Rank-1	Rank-5	mAP
Fixed $\sigma = 1$	88.36	93.63	83.03
Fixed $\sigma = 5$	88.60	93.38	82.96
Fixed $\sigma = 10$	83.58	92.65	79.91
Fixed $\sigma = 100$	69.73	80.88	68.25
Adaptive σ (ours)	89.22	93.50	83.62

Dataset	Market-1501 [13]		
Methods	Rank-1	Rank-5	mAP
Fixed $\sigma = 1$	99.02	99.58	93.56
Fixed $\sigma = 5$	98.81	99.55	93.34
Fixed $\sigma = 10$	98.25	99.41	92.12
Fixed $\sigma = 100$	97.95	99.08	91.91
Adaptive σ (ours)	99.11	99.58	93.80

TABLE III: ReID performance according to the values of σ for the Parzen window method. The best performances are marked in **bold**.

the factor values, as the difference between the maximum mAP and minimum mAP is 0.09%, 1.77%, and 0.47% in VeRi776 [14], Vehicle-3I and Market-1501 [13].

We further compared the ReID performances for the fixed and proposed adaptive σ values. The fixed $\sigma = 1, 5, 10, 100$, and the adaptive σ as in Eq. 2 were tested. As summarized in Table III, the fixed $\sigma = 100$ performed the worst because a too-large σ leads to smoothed distributions close to a uniform distribution and reduces the influence of spatial-temporal information. On the other hand, $\sigma = 1$, $\sigma = 5$ and $\sigma = 10$ performed relatively well. However, compared to using fixed σ values, the proposed adaptive Parzen window with the adaptive σ performed the best in the evaluation metrics (Rank-1, mAP) for all tested datasets. The proposed adaptive Parzen window achieved with 99.70%, 89.22%, 99.11% rank-1 accuracy, and 91.71%, 83.62%, 93.80% mAP on three different datasets, respectively. As explained in Section III-A and Fig. 3, a fixed value of σ has difficulty handling various types of initial histograms h_{ij} . This result implies that setting different σ_{ij} values by considering the various connection strengths of camera pairs is effective and improves ReID performance.

D. Comparison with state-of-the-art methods

In this section, we compare the proposed method with state-of-the-art re-identification methods using the VeRi776 [14], Vehicle-3I vehicle ReID dataset and Market-1501 [13] person ReID dataset. The methods are primarily categorized into two approaches: 1) only appearance-based, 2) using additional spatial-temporal information (marked by †). The methods marked by a ‘*’ performed re-ranking post-processing for the final ReID results.

Table IV summarizes the vehicle ReID results, sorted by rank-1 performance. Our framework achieved outstanding performance in the VeRi776 [14] dataset, performing a rank-1 accuracy of 99.7% and a mAP score of 91.71%. Despite improvements to their baseline methods, the spatial-temporal approaches [8], [14], [30] did not match the performance of other appearance-based methods due to using older appearance models such as SIFT, bag-of-words, and Siamese-CNN for ReID. Furthermore, these methods did not directly estimate the camera network topology or optimize the use of spatial-temporal information.

Many appearance-based methods have significantly improved ReID performance by developing deep learning models. For instance, our baseline appearance model, FastReID [5], achieved a 96.96% rank-1 accuracy and an 81.91% mAP. RPTM [6] notably used the GMS [40] feature matcher and adopted the ResNet-101 [38] structure, demonstrating the superior performance with a 97.3% rank-1 accuracy and an 88.0% mAP. In contrast, despite using a lightweight ResNet-50 structure for the appearance model, our methods outperformed the sophisticated RPTM [6] approach, achieving a 2.4% higher rank-1 accuracy, a 1.42% higher rank-5 accuracy, and a 3.71% higher mAP score. Furthermore, our methods did not perform any re-ranking processes for post-processing.

For Vehicle-3I, several state-of-the-art methods were evaluated. FastReID [5], achieved a 63.73% rank-1 accuracy and 64.24% mAP. On the other hand, CLIP-ReID [21], which achieved the second-best performance on VeRi776, showed the lowest performance on Vehicle-3I because it was trained without viewpoint annotations in this experiment. Adopting Wang’s [10] approach to FastReID [5] achieved 81.37% rank-1 accuracy and 88.60% rank-5 accuracy, proving the effectiveness of spatial-temporal cues. Our method achieved outstanding results, outperforming all other methods with 89.22% rank-1 accuracy and 83.62% mAP. This result showed that using spatial-temporal information with appear-

Dataset	VeRi776 [14]		
Models	Rank-1	Rank-5	mAP
†FACT+Plate-SNN+STR [14]	61.44	78.78	27.77
†Siamese-CNN+Path-LSTM [8]	83.49	90.04	58.27
†PROVID [30]	81.56	95.11	53.42
†KPGST [9]	92.35	93.92	68.73
†FastReID [5] + Wang's [10]	95.77	97.74	85.47
GAN+LSRO* [41]	88.62	94.52	64.78
AAVER* [42]	90.17	94.34	66.35
PAMTRI [43]	92.86	96.97	71.88
SPAN [44]	94.00	97.60	68.90
CAL [45]	95.40	97.90	74.30
PVEN [46]	95.60	98.40	79.50
TBE [47]	96.00	<u>98.50</u>	79.50
TransReID [11]	96.90	-	80.60
VehicleNet* [32]	96.78	-	83.41
SAVER* [48]	96.90	97.70	82.00
DMT* [49]	96.90	-	82.00
FastReID [5]	96.96	98.45	81.91
CLIP-ReID [21]	<u>97.30</u>	-	84.50
Strong Baseline* [29]	97.00	-	87.10
RPTM* [6]	<u>97.30</u>	98.40	<u>88.00</u>
†Ours (Appearance-FastReID [5])	99.70	99.82	91.71
Dataset	Vehicle-3I		
Models	Rank-1	Rank-5	mAP
†FastReID [5] + Wang's [10]	81.37	88.60	66.34
CLIP-ReID [21]	61.90	68.80	59.00
FastReID [5]	63.73	77.70	64.24
†Ours (Appearance-FastReID [5])	89.22	93.50	83.62

TABLE IV: Performance comparisons on Vehicle ReID datasets. † and * indicate the spatial-temporal approach and re-ranking, respectively. The best and second best performances are marked in **bold** and underline.

Models	Rank-1	Rank-5	mAP
GCP [50]	95.2	-	88.9
TransReID [11]	95.2	-	89.5
ISP [28]	95.3	98.6	88.6
GASM [27]	95.3	-	84.7
ABDNET [51]	95.6	-	88.28
SCSN [52]	95.7	-	88.5
CLIP-ReID [21]	95.7	-	89.8
SAN [53]	96.1	-	88.0
FastReID [5]	96.35	-	90.77
PASS [23]	96.9	-	93.3
SOLIDER [19]	96.9	-	93.9
Unsupervised Pre-training [54]	97.0	-	92.0
UP-ReID [22]	97.1	-	91.1
†st-ReID [10]	98.1	99.3	87.6
†Ours (Appearance-FastReID [5])	99.11	<u>99.58</u>	93.8
†Ours (Appearance-SOLIDER [19])	<u>99.0</u>	99.6	95.5

TABLE V: Performance comparisons on the Market-1501 [13] Person ReID dataset. † indicate the spatial-temporal approach, respectively. The best and second best performances are marked in **bold** and underline.

ance information is more effective in difficult conditions than using appearance information only.

The Person ReID results from the Market-1501 [13] dataset are summarized in Table V. Despite the st-ReID [10] achieving a reasonable rank-1 accuracy of 98.1%, the mAP of 87.6% was lower than that of other state-of-the-art methods. On the other hand, SOLIDER [19] with Swin Transformer [20] achieved good performance with an mAP of 93.9%, but its rank-1 performance of 96.9% was relatively low. For this dataset, we selected two different appearance-based models, FastReID [5] and SOLIDER [19], as the baseline

for our framework. As a result, our frameworks achieved the best rank-1 accuracy (99.11%) with FastReID [5], and the best rank-5 accuracy (99.6%) and mAP (95.5%) with SOLIDER [19]. These results imply that the proposed spatial-temporal framework improves both vehicle and person ReID tasks and has the potential to achieve higher performance when it employs a better appearance-based model as its baseline.

Fig. 10 illustrates the qualitative ReID results. We compared the proposed method (Ours) with the baseline method (FastReID [5]), which used only appearance information. The baseline method shows numerous false matches where the appearance closely resembles the query images. The baseline method incorrectly matched ID 470 and 1260 images in Vehicle-3I, which have the same color and model type. However, the proposed method correctly matches most of the same vehicles. In particular, it rarely matched the correct images of the 662-nd vehicle query image in VeRi776 [14] due to many similar black cars. In contrast, the proposed method, thanks to the spatial-temporal information, perfectly matched the correct images at rank-1 to rank-10 under the challenging query and gallery pairs. The baseline model struggled to match correct pairs in the gallery in the person ReID task. For example, ID 342, wearing a stripe yellow shirt, gray shorts, and carrying a black backpack, is easily confused with others wearing similar outfits. ID 1083, wearing a red dress and carrying a shoulder bag, is also very confusing, as another person is wearing a similar red dress with a handbag.

Interestingly, as shown in Fig. 11, the query image is wearing a white shirt and black pants, but it was not wearing an umbrella at that time. Based on the appearance model, it naturally found the images with white shirts and black pants in the gallery. However, the query was wearing an umbrella in other cameras a few minutes later. Under this challenging ReID scenario, the appearance-based model only relies on the appearance of the query and never finds correct matches. In contrast, our method using spatial-temporal information correctly matched the images, even if the appearance of the query has changed significantly. These results support that the proposed ReID (Ours) based on the spatial-temporal fusion network can effectively manage the appearance ambiguity problems and overcome the limitations of the previous ReID methods.

VII. REID IN REAL-WORLD SURVEILLANCE SCENARIOS

A. Settings and evaluation metrics

Unlike the appearance-centric (1-to-all) evaluation settings in Section. VI, in this experiment, we perform ID-to-ID evaluation to consider the real-world scenario. This means that the ReID performances should be evaluated only once for each identity between cameras. For example, each identity has a path across cameras, e.g., $c_1 \rightarrow c_2 \rightarrow c_3 \rightarrow c_4$; thus, ReID methods should correctly track the path based on the ReID between adjacent cameras. For ReID between cameras in the real world, only the rank-1 matching result is valid. Therefore, we considered the rank-1 result with a similarity value over θ_c as a positive matching result. We empirically set $\theta_c = 0.6$.

Dataset	Query ID	Model	Query	Rank-1	Rank-2	Rank-3	Rank-4	Rank-5	Rank-6	Rank-7	Rank-8	Rank-9	Rank-10
VeRi776	ID 30	Baseline											
		Ours											
	ID 150	Baseline											
		Ours											
Vehicle-3I	ID 470	Baseline											
		Ours											
	ID 1260	Baseline											
		Ours											
Market-1501	ID 342	Baseline											
		Ours											
	ID 1083	Baseline											
		Ours											

Fig. 10: Qualitative ReID results of the baseline and proposed methods (Ours). The baseline model [5] is an appearance-based method. Green and red boxes denote true and false matching. Compared to the baseline method, the proposed method can match true positive pairs despite similar appearances and overcome the appearance ambiguities due to the spatial-temporal information (best viewed in color).



Fig. 11: A challenging scenario in ReID. Green and red boxes denote true and false matching. A query image did not carry an umbrella, but it was carrying an umbrella in other cameras (gallery). The baseline (*FastReID* [5]) only relying on appearance information failed to find true matching in the gallery. In contrast, the proposed methods correctly found true matching.

To evaluate the performances, the mean Average Precision (mAP) and F_1 score of predicted object paths are measured. *Vehicle-3I* includes 1,630 training IDs and 408 test IDs, the same as previous experiments in Section. VI. We evaluate our methods in real-world scenarios using *Vehicle-3I* dataset. For evaluation, each test query progressively performs ReID according to the estimated connection matrix. ReID for each query continues until no identities are satisfying $\theta_c > 0.6$ between the test query and its gallery. In this way, the ReID of all test queries is performed, and the performances (mAP, F_1) are measured.

B. Effects of Causal Identity Matching (CIM)

The connection matrix for *Vehicle-3I* dataset can be estimated using the paths of training identities. The size of connection matrix C_{3I} for *Vehicle-3I* is 11×11 . This connection matrix is quite sparse, with only a few adjacent connections between cameras. This means that when performing ReID for the target object, the entire distributions $p_{ij}(t)$ are not needed; only some adjacent $p_{ij}(t)$ are considered at each ReID step. Furthermore, as shown in Fig. 12, the appearances of the target object become much richer through

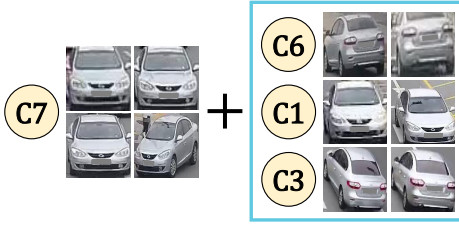


Fig. 12: Appearances of the target object. The appearances in camera 7 (C7) are the initial query. Blue box denotes appearances in difference cameras (C6,C1,C3) after performing Causal Identity Matching (CIM).

Method	mAP	F_1
w/o Causal Identity Matching	93.52	94.14
w/ Causal Identity Matching	94.95	95.19

TABLE VI: ReID performances without and with CIM.

CIM, allowing for more accurate ReID. Although a single camera can only capture fixed poses of the object, progressive query merging easily overcomes this limitation. CIM increases the overall efficiency and accuracy of the ReID system, as summarized in Table VI. This is a very natural procedure, but note that most recent studies have not closely examined such real-world conditions and causality for ReID.

C. Effects of Top- k multi-shot matching

In this experiment, we test the effect of Top- k multi-shot matching between two objects. To this end, we tried different matching strategies as follows:

- Single-shot: performing ReID that only uses a single appearance for each object. For unbiased evaluations, we randomly selected a single appearance for each identity and repeated the appearance selection ten times to average them for the final score.
- Multi-shot (max): matching all possible pairs between multiple appearances and selecting the smallest matching score for the final score as used in [55].
- Multi-shot (avg.): matching all possible pairs between multiple appearances and averaging all matching scores as used in [56].
- Multi-shot (Top- k): proposed method – matching all possible pairs between multiple appearances and averaging only top- k scores.

As summarized in Table. VII, we compared several top- k multi-shot matching methods including $k = 5, 10, 20$, and tested the ReID models FastReID [5] and ours.

In both methods (FastReID [5], Ours), the single-shot matching strategy performed lowest accuracies due to limited appearance cue. Furthermore, using a single appearance for each identity does not correspond to real-world scenarios. Compared to the ‘single-shot’, multi-shot (min) and multi-shot (avg.) strategies achieved higher performances. This results support that using multiple appearance improves the ReID performances. However, multi-shot (max) can be highly

biased in the best similarity score between two sets of appearances. Meanwhile, multi-shot (avg.) can consider multiple comparisons, but the final score can be smoothed out or polluted by unreliable appearances.

On the other hand, the proposed Top- k matching is neither too biased nor too smoothed, and it produces a stable score even when the number of compared appearances changes by appearance management as in proposed in Section IV-B. Regardless of the k value, the proposed Top- k multi-shot matching methods achieved higher performance than other strategies such as single and multi-shot (max, avg.) in both methods (FastReID [5], Ours). It performed 94.95% mAP and 95.19 % F_1 score when the $k = 5$.

D. Effects of appearance management

The complexity of multi-shot matching between two appearance sets is $O(N_m N_n)$, where N_m, N_n are the appearance numbers of m - and n -th objects. This roughly follows a complexity of $O(N^2)$ and needs to be improved for efficiency. Furthermore, among the multiple appearances, many duplicated and polluted appearances lead to performance degradation, as described in Section IV-B. Based on the proposed appearance unreliability score $\mathcal{U}(\mathbf{I}^m)$, we adjusted the number of appearances in each object.

In Table VIII, we tested different settings of the proposed appearance management and performed Top-5 multi-shot matching. The App. selection ratio means the proportion of collected appearances used for ReID. For example, we can use only a few reliable appearances such as 5–50% according to the unreliability score $\mathcal{U}(\mathbf{I}^m)$. App. selection ratio of ‘ALL’ used all collected appearances without performing the proposed appearance management. The proposed appearance management improved the ReID performances about 2% and 1.32% mAP scores for each method (FasetReID, Ours), when they only use 5% reliable appearances, respectively. These results indicate that, regardless of the ReID methods used, ReID performance can be improved with only a few selected appearances. In addition, the matching complexities are dramatically reduced. Additionally, matching complexities are significantly reduced. For example, when selecting only 5% of appearances, 99.75% of redundant calculations can be eliminated, while maintaining or even enhancing performance.

VIII. CONCLUSION

In this study, we proposed a ReID framework based on a spatial-temporal fusion network and causal identity matching (CIM), which considers the issues in real-world scenarios. The proposed framework estimates camera network topology and combines appearance and spatial-temporal similarities to reduce appearance ambiguity. To this end, we proposed an adaptive Parzen window for reliable topology estimation and FusionNet for optimal similarity aggregation. The proposed framework demonstrates outstanding performances on the VeRi776 [14], Vehicle-3I and Market-1501 [13] datasets, achieving 99.70%, 89.22%, and 99.11% rank-1 accuracy and 91.71%, 83.62%, and 95.5% mAP, respectively. The results indicate that incorporating spatial and temporal

Datasets		Vehicle-3I	
Models	Matching methods	mAP	F_1 score
FastReID [5]	single-shot	79.71	80.08
	multi-shot (max)	86.32	86.55
	multi-shot (avg.)	87.14	87.45
	multi-shot (Top-5)	87.46	87.73
	multi-shot (Top-10)	88.11	88.42
	multi-shot (Top-20)	88.55	88.90
Ours	single-shot	88.75	89.24
	multi-shot (max)	94.30	94.57
	multi-shot (avg.)	91.15	91.65
	multi-shot (Top-5)	94.95	95.19
	multi-shot (Top-10)	94.17	94.48
	multi-shot (Top-20)	94.17	94.54

TABLE VII: Performance comparisons of various matching strategies on the Vehicle-3I dataset. Single-shot and multi-shot (max, avg.) are the traditional ReID matching strategies, and multi-shot (top- k) is our proposed matching method. The best performances are marked in **bold**.

Datasets		Vehicle-3I	
Models	App. selection ratio	mAP	F_1 score
FastReID [5]	ALL	85.47	85.72
	50 %	84.80	85.02
	20 %	86.57	86.81
	10 %	87.22	87.49
	5 %	87.46	87.73
Ours	ALL	93.63	93.85
	50 %	91.91	92.24
	20 %	93.95	94.24
	10 %	94.77	94.93
	5 %	94.95	95.19

TABLE VIII: ReID performance according to the App. selection ratio for the proposed appearance management on the Vehicle-3I dataset. Best performances are marked in **bold**.

information in ReID can improve the accuracy of appearance-based methods and effectively address appearance ambiguity.

Additionally, we proposed causal identity matching (CIM) to consider the issues in real-world scenarios. The proposed CIM uses adjacent cameras and transition time distributions to dynamically assign gallery sets for target objects to include only relevant objects and progressively merge queries to improve ReID accuracy and variety. In Vehicle-3I dataset, proposed CIM achieved outstanding performances by 94.95% mAP and 95.19% F_1 score. The results demonstrate that the proposed CIM is effective in real-world surveillance scenarios beyond the laboratory setting. Although the proposed ReID framework has lightweight networks, it can effectively perform ReID tasks. Furthermore, the proposed CIM is flexible enough to use other ReID frameworks and appearance-based methods.

REFERENCES

[1] E. Ahmed, M. Jones, and T. K. Marks, "An improved deep learning architecture for person re-identification," in *CVPR*, 2015, pp. 3908–3916.

[2] Y. Chen, X. Zhu, and S. Gong, "Person re-identification by deep learning multi-scale representations," in *Proceedings of the IEEE international conference on computer vision workshops*, 2017, pp. 2590–2600.

[3] W.-S. Zheng, S. Gong, and T. Xiang, "Person re-identification by probabilistic relative distance comparison," in *CVPR*. IEEE, 2011, pp. 649–656.

[4] M. Koestinger, M. Hirzer, P. Wohlhart, P. M. Roth, and H. Bischof, "Large scale metric learning from equivalence constraints," in *CVPR*. IEEE, 2012, pp. 2288–2295.

[5] L. He, X. Liao, W. Liu, X. Liu, P. Cheng, and T. Mei, "Fastreid: A pytorch toolbox for general instance re-identification," *arXiv preprint arXiv:2006.02631*, 2020.

[6] A. Ghosh, K. Shanmugalingam, and W.-Y. Lin, "Relation preserving triplet mining for stabilising the triplet loss in re-identification systems," in *Proceedings of the IEEE/CVF Winter Conference on Applications of Computer Vision*, 2023, pp. 4840–4849.

[7] Y.-J. Cho, S.-A. Kim, J.-H. Park, K. Lee, and K.-J. Yoon, "Joint person re-identification and camera network topology inference in multiple cameras," *Computer Vision and Image Understanding*, vol. 180, pp. 34–46, 2019.

[8] Y. Shen, T. Xiao, H. Li, S. Yi, and X. Wang, "Learning deep neural networks for vehicle re-id with visual-spatio-temporal path proposals," in *ICCV*, 2017, pp. 1900–1909.

[9] W. Huang, X. Zhong, X. Jia, W. Liu, M. Feng, Z. Wang, and S. Satoh, "Vehicle re-identification with spatio-temporal model leveraging by pose view embedding," *Electronics*, vol. 11, no. 9, p. 1354, 2022.

[10] G. Wang, J. Lai, P. Huang, and X. Xie, "Spatial-temporal person re-identification," in *Proceedings of the AAAI conference on artificial intelligence*, vol. 33, no. 01, 2019, pp. 8933–8940.

[11] S. He, H. Luo, P. Wang, F. Wang, H. Li, and W. Jiang, "Transreid: Transformer-based object re-identification," in *ICCV*, 2021, pp. 15 013–15 022.

[12] H.-G. Kim, Y. Na, H.-W. Joe, Y.-H. Moon, and Y.-J. Cho, "Spatial-temporal vehicle re-identification," *arXiv preprint arXiv:2309.01166*, 2023.

[13] L. Zheng, L. Shen, L. Tian, S. Wang, J. Wang, and Q. Tian, "Scalable person re-identification: A benchmark," in *Computer Vision, IEEE International Conference on*, 2015.

[14] X. Liu, W. Liu, T. Mei, and H. Ma, "A deep learning-based approach to progressive vehicle re-identification for urban surveillance," in *Computer Vision—ECCV 2016: 14th European Conference, Amsterdam, The Netherlands, October 11–14, 2016, Proceedings, Part II 14*. Springer, 2016, pp. 869–884.

[15] D. Cheng, Y. Gong, S. Zhou, J. Wang, and N. Zheng, "Person re-identification by multi-channel parts-based cnn with improved triplet loss function," in *CVPR*, 2016, pp. 1335–1344.

[16] A. Hermans, L. Beyer, and B. Leibe, "In defense of the triplet loss for person re-identification," *arXiv preprint arXiv:1703.07737*, 2017.

[17] L. Rong, Y. Xu, X. Zhou, L. Han, L. Li, and X. Pan, "A vehicle re-identification framework based on the improved multi-branch feature fusion network," *Scientific Reports*, vol. 11, no. 1, p. 20210, 2021.

[18] S. Khamis, C.-H. Kuo, V. K. Singh, V. D. Shet, and L. S. Davis, "Joint learning for attribute-consistent person re-identification," in *Computer Vision—ECCV 2014 Workshops: Zurich, Switzerland, September 6–7 and 12, 2014, Proceedings, Part III 13*. Springer, 2015, pp. 134–146.

[19] W. Chen, X. Xu, J. Jia, H. Luo, Y. Wang, F. Wang, R. Jin, and X. Sun, "Beyond appearance: a semantic controllable self-supervised learning framework for human-centric visual tasks," in *CVPR*, 2023, pp. 15 050–15 061.

[20] Z. Liu, Y. Lin, Y. Cao, H. Hu, Y. Wei, Z. Zhang, S. Lin, and B. Guo, "Swin transformer: Hierarchical vision transformer using shifted windows," in *ICCV*, 2021, pp. 10 012–10 022.

[21] S. Li, L. Sun, and Q. Li, "Clip-reid: Exploiting vision-language model for image re-identification without concrete text labels," in *Proceedings of the AAAI Conference on Artificial Intelligence*, vol. 37, no. 1, 2023, pp. 1405–1413.

[22] Z. Yang, X. Jin, K. Zheng, and F. Zhao, "Unleashing potential of unsupervised pre-training with intra-identity regularization for person re-identification," in *CVPR*, 2022, pp. 14 298–14 307.

[23] K. Zhu, H. Guo, T. Yan, Y. Zhu, J. Wang, and M. Tang, "Pass: Part-aware self-supervised pre-training for person re-identification," in *European Conference on Computer Vision*. Springer, 2022, pp. 198–214.

[24] Y.-J. Cho and K.-J. Yoon, "Improving person re-identification via pose-aware multi-shot matching," in *CVPR*, 2016, pp. 1354–1362.

[25] C. Su, J. Li, S. Zhang, J. Xing, W. Gao, and Q. Tian, "Pose-driven deep convolutional model for person re-identification," in *ICCV*, 2017, pp. 3960–3969.

- [26] J. Miao, Y. Wu, P. Liu, Y. Ding, and Y. Yang, "Pose-guided feature alignment for occluded person re-identification," in *ICCV*, 2019, pp. 542–551.
- [27] L. He and W. Liu, "Guided saliency feature learning for person re-identification in crowded scenes," in *Computer Vision–ECCV 2020: 16th European Conference, Glasgow, UK, August 23–28, 2020, Proceedings, Part XXVIII 16*. Springer, 2020, pp. 357–373.
- [28] K. Zhu, H. Guo, Z. Liu, M. Tang, and J. Wang, "Identity-guided human semantic parsing for person re-identification," in *Computer Vision–ECCV 2020: 16th European Conference, Glasgow, UK, August 23–28, 2020, Proceedings, Part III 16*. Springer, 2020, pp. 346–363.
- [29] S. V. Huynh, "A strong baseline for vehicle re-identification," in *CVPR*, 2021, pp. 4147–4154.
- [30] X. Liu, W. Liu, T. Mei, and H. Ma, "Provid: Progressive and multi-modal vehicle reidentification for large-scale urban surveillance," *IEEE Transactions on Multimedia*, vol. 20, no. 3, pp. 645–658, 2017.
- [31] K. Lv, H. Du, Y. Hou, W. Deng, H. Sheng, J. Jiao, and L. Zheng, "Vehicle re-identification with location and time stamps," in *CVPR workshops*, 2019, pp. 399–406.
- [32] Z. Zheng, T. Ruan, Y. Wei, Y. Yang, and T. Mei, "Vehiclenet: Learning robust visual representation for vehicle re-identification," *IEEE Transactions on Multimedia*, vol. 23, pp. 2683–2693, 2020.
- [33] M. Ren, L. He, X. Liao, W. Liu, Y. Wang, and T. Tan, "Learning instance-level spatial-temporal patterns for person re-identification," in *ICCV*, 2021, pp. 14 930–14 939.
- [34] Y.-J. Cho and D. Kim, "Rethinking multi-object tracking based on re-identification and appearance model management," *IEEE Access*, vol. 11, pp. 54 337–54 351, 2023.
- [35] J. Li, S. Zhang, and T. Huang, "Multi-scale 3d convolution network for video based person re-identification," in *Proceedings of the AAAI conference on artificial intelligence*, vol. 33, no. 01, 2019, pp. 8618–8625.
- [36] T. Zhang, L. Wei, L. Xie, Z. Zhuang, Y. Zhang, B. Li, and Q. Tian, "Spatiotemporal transformer for video-based person re-identification," *arXiv preprint arXiv:2103.16469*, 2021.
- [37] A. V. Aho, M. R. Garey, and J. D. Ullman, "The transitive reduction of a directed graph," *SIAM Journal on Computing*, vol. 1, no. 2, pp. 131–137, 1972.
- [38] K. He, X. Zhang, S. Ren, and J. Sun, "Deep residual learning for image recognition," in *CVPR*, 2016, pp. 770–778.
- [39] G. Wang, Y. Yuan, X. Chen, J. Li, and X. Zhou, "Learning discriminative features with multiple granularities for person re-identification," in *Proceedings of the 26th ACM international conference on Multimedia*, 2018, pp. 274–282.
- [40] J. Bian, W.-Y. Lin, Y. Matsushita, S.-K. Yeung, T.-D. Nguyen, and M.-M. Cheng, "Gms: Grid-based motion statistics for fast, ultra-robust feature correspondence," in *CVPR*, 2017, pp. 4181–4190.
- [41] F. Wu, S. Yan, J. S. Smith, and B. Zhang, "Joint semi-supervised learning and re-ranking for vehicle re-identification," in *2018 24th International Conference on Pattern Recognition (ICPR)*. IEEE, 2018, pp. 278–283.
- [42] P. Khorramshahi, A. Kumar, N. Peri, S. S. Rambhatla, J.-C. Chen, and R. Chellappa, "A dual-path model with adaptive attention for vehicle re-identification," in *ICCV*, 2019, pp. 6132–6141.
- [43] Z. Tang, M. Naphade, S. Birchfield, J. Tremblay, W. Hodge, R. Kumar, S. Wang, and X. Yang, "Pamtri: Pose-aware multi-task learning for vehicle re-identification using highly randomized synthetic data," in *ICCV*, 2019, pp. 211–220.
- [44] T.-S. Chen, C.-T. Liu, C.-W. Wu, and S.-Y. Chien, "Orientation-aware vehicle re-identification with semantics-guided part attention network," in *Computer Vision–ECCV 2020: 16th European Conference, Glasgow, UK, August 23–28, 2020, Proceedings, Part II 16*. Springer, 2020, pp. 330–346.
- [45] Y. Rao, G. Chen, J. Lu, and J. Zhou, "Counterfactual attention learning for fine-grained visual categorization and re-identification," in *ICCV*, 2021, pp. 1025–1034.
- [46] D. Meng, L. Li, X. Liu, Y. Li, S. Yang, Z.-J. Zha, X. Gao, S. Wang, and Q. Huang, "Parsing-based view-aware embedding network for vehicle re-identification," in *CVPR*, 2020, pp. 7103–7112.
- [47] W. Sun, G. Dai, X. Zhang, X. He, and X. Chen, "Tbe-net: A three-branch embedding network with part-aware ability and feature complementary learning for vehicle re-identification," *IEEE Transactions on Intelligent Transportation Systems*, vol. 23, no. 9, pp. 14 557–14 569, 2021.
- [48] P. Khorramshahi, N. Peri, J.-c. Chen, and R. Chellappa, "The devil is in the details: Self-supervised attention for vehicle re-identification," in *Computer Vision–ECCV 2020: 16th European Conference, Glasgow, UK, August 23–28, 2020, Proceedings, Part XIV 16*. Springer, 2020, pp. 369–386.
- [49] S. He, H. Luo, W. Chen, M. Zhang, Y. Zhang, F. Wang, H. Li, and W. Jiang, "Multi-domain learning and identity mining for vehicle re-identification," in *Proceedings of the IEEE/CVF Conference on Computer Vision and Pattern Recognition Workshops*, 2020, pp. 582–583.
- [50] H. Park and B. Ham, "Relation network for person re-identification," in *Proceedings of the AAAI conference on artificial intelligence*, vol. 34, no. 07, 2020, pp. 11 839–11 847.
- [51] T. Chen, S. Ding, J. Xie, Y. Yuan, W. Chen, Y. Yang, Z. Ren, and Z. Wang, "Abd-net: Attentive but diverse person re-identification," in *ICCV*, 2019, pp. 8351–8361.
- [52] X. Chen, C. Fu, Y. Zhao, F. Zheng, J. Song, R. Ji, and Y. Yang, "Saliency-guided cascaded suppression network for person re-identification," in *CVPR*, 2020, pp. 3300–3310.
- [53] X. Jin, C. Lan, W. Zeng, G. Wei, and Z. Chen, "Semantics-aligned representation learning for person re-identification," in *Proceedings of the AAAI Conference on Artificial Intelligence*, vol. 34, no. 07, 2020, pp. 11 173–11 180.
- [54] D. Fu, D. Chen, J. Bao, H. Yang, L. Yuan, L. Zhang, H. Li, and D. Chen, "Unsupervised pre-training for person re-identification," in *CVPR*, 2021, pp. 14 750–14 759.
- [55] M. Farenzena, L. Bazzani, A. Perina, V. Murino, and M. Cristani, "Person re-identification by symmetry-driven accumulation of local features," in *Proceedings of the IEEE Conference on Computer Vision and Pattern Recognition*. IEEE, 2010, pp. 2360–2367.
- [56] Y. Li, Z. Wu, and R. J. Radke, "Multi-shot re-identification with random-projection-based random forests," in *IEEE Winter Conference on Applications of Computer Vision*. IEEE, 2015, pp. 373–380.